

Optical and Spin Coherence Properties of Nitrogen-Vacancy Centers Placed in a 100 nm Thick Isotopically Purified Diamond Layer

Toyofumi Ishikawa,[†] Kai-Mei C. Fu,[‡] Charles Santori,[§] Victor M. Acosta,[§] Raymond G. Beausoleil,[§] Hideyuki Watanabe,^{||} Shinichi Shikata,^{||} and Kohei M. Itoh^{*,†}

[†]Graduate School of Fundamental Science and Technology, Keio University, Yokohama 223-8522, Japan

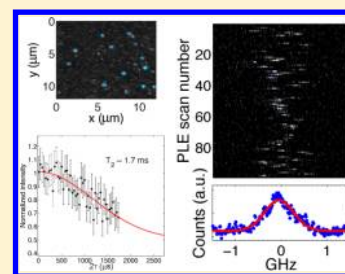
[‡]Department of Physics and Department of Electrical Engineering, University of Washington, Seattle, Washington 98195, United States

[§]Information and Quantum Systems Lab, Hewlett–Packard Laboratories, 1501 Page Mill Road, Palo Alto, 94304, California, United States

^{||}Diamond Research Laboratory, National Institute of Advanced Industrial Science and Technology (AIST), Tsukuba Central 2-13, 1-1-1, Umezono, Tsukuba, Ibaraki 305-8568, Japan

S Supporting Information

ABSTRACT: We have studied optical and spin properties of near-surface nitrogen-vacancy (NV) centers incorporated during chemical vapor phase growth of isotopically purified ¹²C single-crystal diamond layers. The spectral diffusion-limited line width of zero-phonon luminescence from the NV centers is 1.2 ± 0.5 GHz, a considerable improvement over that of NV centers formed by ion implantation and annealing. Enhanced spin dephasing times ($T_2^* \approx 90 \mu\text{s}$, $T_2 \approx 1.7$ ms) due to the reduction of ¹³C nuclear spins persist even for NV centers placed within 100 nm of the surface.



KEYWORDS: diamond, nitrogen-vacancy center, chemical vapor deposition, quantum information processing, magnetometry

In recent years, quantum information processing (QIP) based on nitrogen-vacancy (NV) centers in diamond has seen much progress.^{1,2} The spin-dependent optical properties of NV centers allow optical readout³ and manipulation⁴ of the spin states, coherent population trapping,⁵ and entanglement between photons and the spin qubits.⁶ Since the NV center exhibits a long electron-spin coherence time,⁷ it is also a promising system for applications in quantum memory^{8–10} and magnetometry.^{11–15}

For diamond-based QIP and magnetometry, it is often desirable for NV centers to be located within nanometers of the diamond surface. For QIP, near-surface NV centers enable efficient optical coupling to on-chip waveguides and cavities.^{16–20} For nanoscale magnetometry, near-surface NV centers will reduce the sensor-sample distance, thereby improving sensitivity. The most well-studied way to create near-surface NV centers is a procedure based on ion implantation and annealing.^{21–23} However, these NV centers suffer from large optical spectral diffusion prohibiting efficient spin readout and spin-photon entanglement.^{6,24,25} Furthermore, the coherence times of these defects are much shorter than those found for NV centers formed during crystal growth.²⁶ This suggests that a promising approach to producing near-surface NV centers is to incorporate the centers during the growth of a thin epitaxial layer. In this work, we study the optical and spin coherence properties of such growth-incorporated centers in an isotopically purified ¹²C film.

Promisingly, we find the spectral diffusion of the zero-phonon line (ZPL) is significantly improved, when compared to implanted samples. Moreover, we find that the long spin coherence times expected for ¹²C diamond persist even for NV centers within 100 nm of the surface. These properties indicate that NV centers in such thin layers are promising for applications in both QIP and magnetometry.

We used two samples named S1 and S2. The ¹²C diamond layers (¹²C] = 99.99%) of S1 and S2 were deposited on synthetic type IIa (100) single-crystal diamond plates by microwave plasma assisted chemical vapor deposition (CVD). The growth conditions are described in our Supporting Information. The resulting ¹²C layer thickness is 1000 nm for S1, and 525 nm for S2. In sample S1, nitrogen gas was introduced during the last 100 nm of growth to intentionally create NV centers.

In the first experiment, we performed scanning confocal microscopy operating at room temperature to confirm that NV center luminescence originates from a single thin layer. 532 nm laser light was used for excitation, and photoluminescence (PL) from the negatively charged NV (NV⁻) phonon sidebands (650–800 nm) was collected through a 0.9 numerical aperture microscope objective.

Received: January 27, 2012

Revised: February 25, 2012

Published: March 9, 2012

Figure 1a shows a $12 \times 12 \mu\text{m}^2$ scanning confocal image on the S1 surface (xy -scan). A depth profile (xz -scan) in Figure 1b

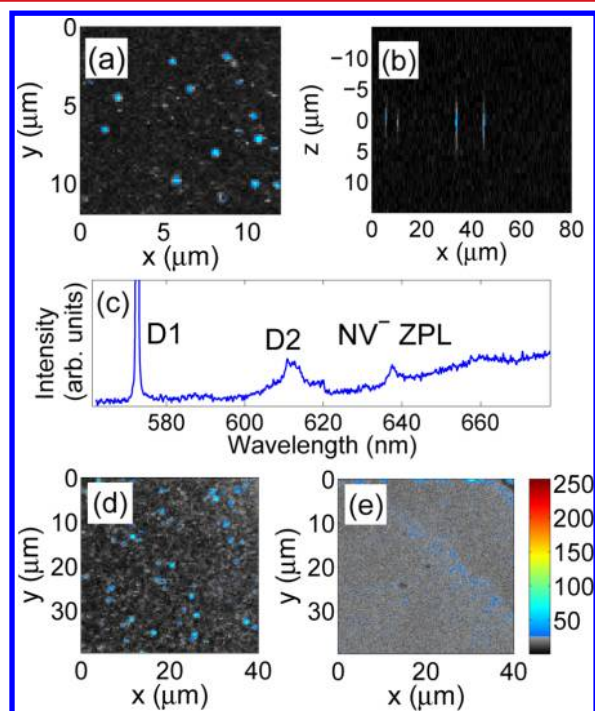


Figure 1. (a) Confocal PL image on the S1 surface (xy -scan). (b) Confocal xz -scan. The light is focused on the sample surface at $z \sim 0$ and $z > 0$ denotes focal positions inside the sample. The z -axis is scaled by the diamond refractive index ($n = 2.4$). The spatial resolution in the x – y plane is approximately the laser spot size (500 nm) and that in z -direction is $3 \mu\text{m}$. Therefore, the NV positions appear as smeared narrow vertical lines. (c) PL spectrum from a representative NV in (a). D1 and D2 indicate the first and second-order diamond Raman peaks. (d) $40 \times 40 \mu\text{m}^2$ confocal PL image on the S1 surface before etching. Fluorescence spots correspond to NV centers. (e) Confocal images on the S1 surface after etching the N-doped layer. The color-bar legend is defined in terms of photon counts per millisecond.

shows that the fluorescent spots are located near the sample surface ($z = 0$), while the substrate remains dark. Room-temperature PL spectra from the individual fluorescence spots show a peak at 638 nm corresponding to the NV^- zero-phonon line (ZPL) (Figure 1c). We measured 150 NV centers in S1 and found that 142 NV centers were located in a plane of width less than the z -axial resolution = $3 \mu\text{m}$ (Supporting Information). By counting single NV defects in several confocal images, we estimate that the concentration of the NV centers is $(5.0 \pm 2.8) \times 10^{10} \text{ cm}^{-3}$.

To confirm that the NV centers are located inside the nitrogen-doped layer of S1, we studied the NV luminescence before and after etching the S1 sample surface. The majority of the sample was masked with 10 nm of titanium followed by 90 nm of SiO_2 , leaving a region of NV centers unmasked. Inductively coupled reactive ion etching (ICP-RIE) with Ar/O_2 chemistry for 120 s was performed. The etch depth, measured by a profilometer, varied from 80 to 140 nm over the unmasked area. Figure 1d,e shows confocal PL images of the unmasked area before and after the etch. The fluorescence spots in Figure 1d correspond to the NV centers, while no NV luminescence is observed after the etch, indicated by Figure 1e. Therefore, these measurements confirm that the NV centers are located within

the top 140 nm of the surface and indicate that they were incorporated during the intentional N-doped growth.

In the second experiment, we performed low-temperature photoluminescence excitation (PLE) spectroscopy on single NV centers in S1 to measure their zero-phonon optical transition linewidths. In the PLE measurement, a tunable external-cavity diode laser was scanned across the ZPL transition (637 nm) while collecting the phonon sideband emission (650–800 nm). The sample was mounted on the copper coldfinger of an ultrahigh vacuum liquid-helium cryostat. Before each scan, a 532 nm pulse was applied to reverse photoionization which eventually occurs with 637 nm excitation alone.²⁷

Figure 2a shows a series of representative PLE scans, and we observed that the central frequency of the resonance peak was

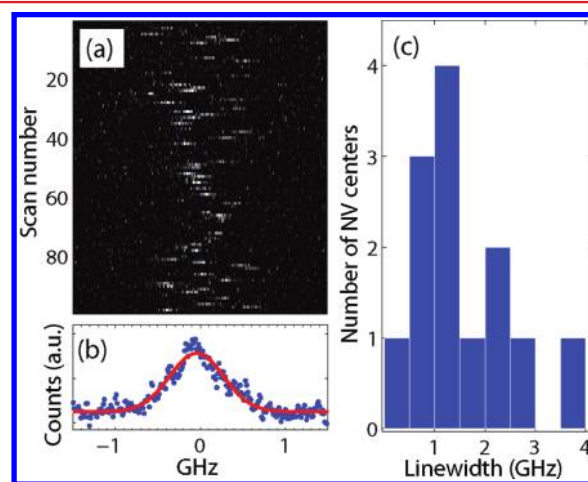


Figure 2. PLE results of NV centers in S1 at 15K. (a) A series of representative PLE scans. Before every scan, the repump laser was applied. (b) Sum of all PLE scans in (a). Blue points and a red solid line are experimental data and the Gaussian fit (fwhm = 0.75 GHz). (c) Statistical data of fwhm obtained from 13 NV centers.

shifted in every scan. The single-scan line width is ~ 100 MHz, while the central frequency is observed to shift several hundred megahertz between subsequent scans. The shifts of the central frequency make a cumulative full width at half-maximum (fwhm) line width of 0.75 GHz as shown in Figure 2b. Figure 2c shows a histogram of results from a similar analysis applied to PLE data from 13 NV centers in S1. We find with the scanning speed of 12 GHz/sec that the average line width is 1.2 GHz with a standard deviation of 0.5 GHz. To eliminate the possibility of the local laser heating shifting the frequency, we have changed the duration of each scan to confirm that the line width stays the same. Typically, spectral diffusion of the zero-phonon optical transition from near-surface NV centers formed by ion implantation and annealing is of the order of 10 GHz.²¹ Measurement-based quantum information schemes require the efficient collection and detection of spectrally identical NV-emitted photons. This practically requires nanoscale device integration and thus near-surface NV centers. Our optical line width results indicate that near-surface NV centers formed during the growth process are promising for measurement-based QIP schemes.

In the third experiment, we measured the time-averaged dephasing time T_2^* of single NV centers at room temperature using optically detected magnetic resonance (ODMR) spectroscopy.^{28,29} The term T_2^* usually represents inhomogeneous

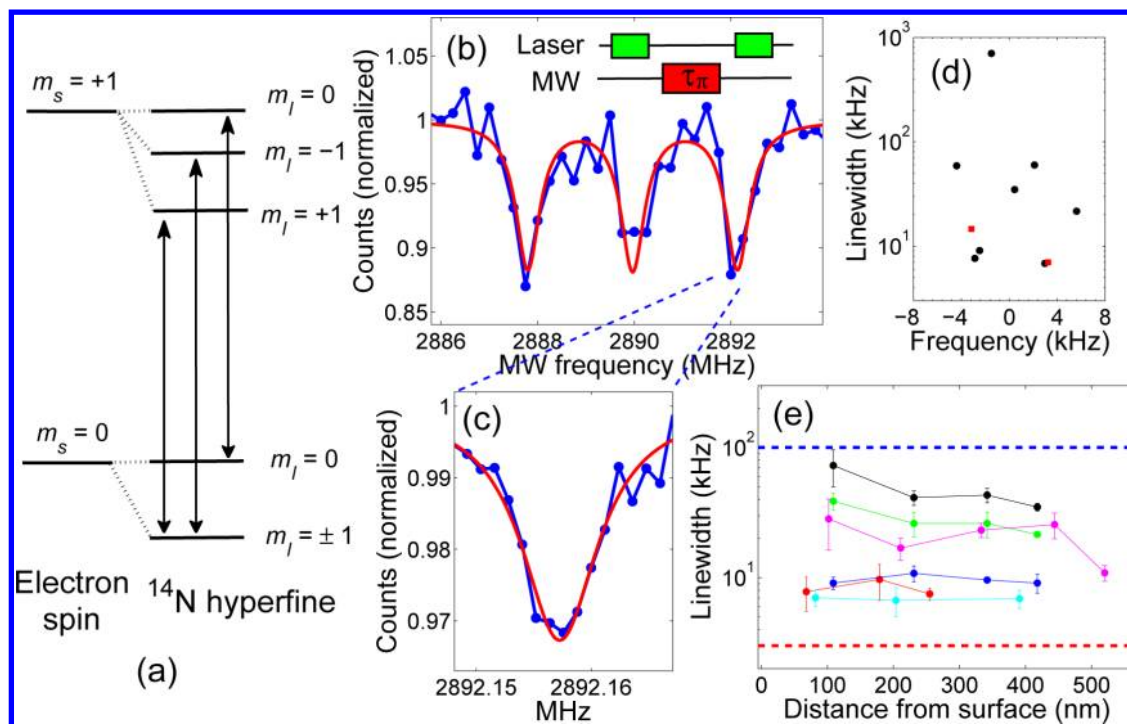


Figure 3. (a) Energy level diagram for the NV ground state including the hyperfine splitting due to the ^{14}N nuclear spin. There are three allowed MW transitions ($\Delta m_I = 0$). The $m_s = -1$ state is not included. (b) Pulsed-ODMR spectrum of a single NV center in S2 with $\tau_\pi = 1 \mu\text{s}$. A three-peak Lorentzian fit (red) gives the expected 2.2 MHz ^{14}N hyperfine splitting.^{30–32} The inset depicts the optical and MW pulse sequences. (c) High-resolution pulsed-ODMR measurement of the highest-energy dip in (b) with $\tau_\pi = 312 \mu\text{s}$. A Lorentzian fit (red) to the peak yields fwhm = 8 kHz. (d) Scatter plot of the line width and transition frequency from each of the 10 NV centers studied in S2. Red squares indicate doublet structure was observed and the transition frequency is taken as the average frequency (see text). (e) Pulsed-ODMR line width of several NV centers as a function of distance from the surface. Each curve corresponds to a single NV center, and we measured these single NV centers several times following etching. A red dashed line is the lowest possible line width due to MW broadening (Supporting Information). A blue dashed line indicates the typical pulsed-ODMR line width of NV centers in ^{13}C diamond.^{7,28,35}

dephasing time that is characteristic of an ensemble of spins. However, when a single spin is measured repeatedly, it will also suffer from temporally averaged dephasing, which can be categorized as T_2^* . T_2^* is a critical figure of merit as it determines DC magnetic sensitivity and quantum information storage time in the absence of refocusing techniques. Furthermore, the transition frequency distribution for many NV centers, Δf_{ens} , determines the broadband magnetic sensitivity for an ensemble of NV centers. It is advantageous to use ^{12}C diamond for ensemble magnetometry if the inhomogeneous magnetic resonance line width is narrower than that of ^{13}C .

A 7 G magnetic field was applied to sample S2 in order to split the $m_s = \pm 1$ electron sublevels. As depicted in Figure 3a, the electron sublevels are further split by the hyperfine interaction with the ^{14}N spin resulting in three possible transitions ($\Delta m_I = 0$) between $m_s = +1$ and $m_s = 0$. Ten NV centers with their NV axes aligned within 10 degrees of the applied magnetic field were studied.

The transition line width was measured by pulsed-ODMR spectroscopy to estimate T_2^* .^{28,29} A schematic of the pulsed-ODMR experiment is depicted in the inset of Figure 3b. A green laser pulse (532 nm, 1.5 μs) is first used to optically pump the NV center into the $m_s = 0$ state. A MW pulse with length τ_π , corresponding to a $m_s = 0 \rightarrow m_s = 1$ transition on resonance, is then applied. As this sequence repeats, the green laser pulse is used both to read out the spin state (first 500 ns) and to optically pump the NV center for the next cycle. In the NV system, the fluorescence intensity under green excitation is

dependent on the electron spin projection (brighter for $m_s = 0$, weaker for $m_s = \pm 1$). Thus, the ODMR spectrum is measured by monitoring the readout fluorescence as the MW frequency is tuned through the magnetic resonance manifold. In the case where $\tau_\pi \ll T_2^*$ we expect complete transfer from the $m_s = 0$ to the $m_s = 1$ state on resonance, the maximum possible contrast in the pulsed-ODMR spectrum, and an ODMR line width limited by the bandwidth of the MW pulse. If $\tau_\pi \geq T_2^*$ we expect the contrast to decrease and the line width to approach $1/\pi T_2^*$.²⁸

In Figure 3b,c, we show typical pulsed-ODMR spectra for different MW powers. In Figure 3b, a $\tau_\pi = 1 \mu\text{s}$ pulse is scanned over the $m_s = +1 \leftrightarrow m_s = 0$ manifold. A three-peak Lorentzian fit yields a hyperfine splitting of 2.2 MHz as expected.^{30–32} In this particular spectrum the 0.6 MHz line width is limited by the MW bandwidth. We repeat the experiment with a significantly lower MW power ($\tau_\pi = 312 \mu\text{s}$) and scan over the highest-energy resonance (Figure 3c). The measured line width is 8 kHz, which is significantly broader than the 3 kHz contribution due to the finite MW pulse length (Supporting Information). To estimate T_2^* , we used numerical simulations based on a two-level density matrix for fitting to the pulsed-ODMR spectra. The resulting maximum T_2^* is $\sim 90 \mu\text{s}$ corresponding to the 7 kHz observed line width. Details are provided in our Supporting Information.

The observed linewidths and resonant frequencies for all 10 NVs are shown in Figure 3d. We note that two NV centers exhibited two ODMR dips instead of the single dip observed in Figure 3c. The doublet splittings observed were 50 and 20 kHz

and are presumably due to the hyperfine interaction with a residual ^{13}C nucleus.^{29,33} We observe variation in the pulsed-ODMR linewidths with all but one NV center exhibiting a line width in the 7–60 kHz range (the outlier had a line width of ~ 700 kHz). As discussed further below, the variation in line width is consistent with variation in the local environment of each NV center. Since the transition frequency distribution Δf_{ens} is much narrower than the 7 kHz line width, such NV centers are promising for ensemble magnetometry.

There are several factors that could contribute to the measured transition linewidths. One possibility is dipole–dipole interaction with surface paramagnetic surface defects. We thus studied the ODMR transition line width as a function of NV distance from the surface. The NV depth was determined by etching the sample surface and studying the NV luminescence.²¹ The majority of the sample was masked with 130 nm of SiO_2 deposited by e-beam evaporation leaving the region containing the NV centers unmasked. The sample was then etched in 20–30 nm steps by ICP-RIE. An Ar/Cl_2 etch chemistry for 20 s followed by an Ar/O_2 chemistry for 75 s was used for each 20–30 nm step. After each etch step, the mask thickness was measured by ellipsometry and the total etch distance was measured by a profilometer. Next, confocal microscopy was performed to determine whether each NV was still optically active. After every 4 etch steps (~ 100 nm), pulsed-ODMR measurements were performed on each NV center to determine the resonance line width. As shown in Figure 3e, we observe no significant dependence of the ODMR line width on the NV depth for NVs at least 70 nm from the surface (the minimum distance for an NV in this experiment). This is strong evidence that surface spins are making a negligible contribution to the pulsed-ODMR linewidths.

Interaction due to paramagnetic defects within the crystal is the most probable cause of the line width distribution we observe. When a paramagnetic impurity such as nitrogen is located approximately 15 nm (30 nm) from the NV center, dipole–dipole interaction generates 100 kHz (10 kHz) linewidths.^{12,14} Even the narrowest lines observed, 7 kHz, are most likely limited by interaction with paramagnetic impurities. The broadening due to the residual 0.01% ^{13}C is expected to contribute only 1 kHz.^{12,14,35} Magnetic field drift and fluctuations due to the magnet current supply should contribute less than 0.1 kHz to the linewidths. To minimize temperature dependence of the ODMR center frequency, the diamond sample was temperature stabilized to within 0.01 C with a Peltier cooler which corresponds to <1 kHz contribution.³⁴

Finally, we performed spin echo measurements on a single NV center in the S1 sample at room temperature by using the following MW-pulse sequence; $\pi/2-\tau-\pi-\tau-\pi/2$. A 532 nm excitation pulse was applied for the spin polarization before the MW sequence, and the spin echo sequence was repeated for a range of free spin evolution periods (τ). The final MW pulse ($\pi/2$) in the sequence was used to project a superposition state between $m_s = 0$ and $m_s = 1$ states into a population difference, which is detected through the spin-dependent luminescence. The green excitation pulse was then applied for the detection of the spin states and repolarization and then the sequence was repeated.

Figure 4 is the spin echo result as a function of τ . From fitting a Gaussian dependence, $\exp[-(2\tau/T_2)^2]$,⁷ we estimate $T_2 = 1.7 \pm 0.1$ ms. Since this is much longer than the coherence time of NV centers in high-purity natural abundance diamond ($T_2 =$

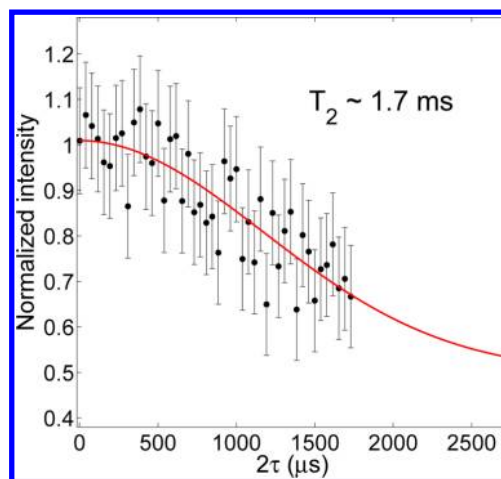


Figure 4. Spin echo results from a NV center in the S1 sample. Black filled circles are experimental spin echo data, and each error bar is estimated by shot noise. Average over first 10 data points is used for normalization. A red curve fitted by $\exp[-(2\tau/T_2)^2]$ gives $T_2 = 1.7 \pm 0.1$ ms.

$350 \mu\text{s}$),³⁶ our spin echo results show that the enhanced spin coherence lifetimes observed in bulk ^{12}C samples can be observed as well for NV centers placed within 100 nm of the surface.

In summary, we have studied optical and spin properties of NV centers in a thin isotopically controlled ^{12}C diamond layer. The spectral diffusion-limited optical linewidths of the NV centers are significantly narrower than those of NV centers formed by implantation and annealing. Our pulsed-ODMR spectroscopy has found that variations in the local magnetic environment around single NV centers result in a distribution of dephasing times up to $T_2^* \sim 90 \mu\text{s}$. For magnetic sensing applications, this corresponds to a DC field spin-projection-noise limited sensitivity of $1.9 \text{ nT Hz}^{-1/2}$.^{7,12,14} Thus, we envision using NV centers in intentionally doped, isotopically pure CVD diamond for nanoscale magnetometry, to obtain simultaneously high spatial resolution and sensitivity.¹² Furthermore, our spin echo results show that a near-surface NV center has electron-spin coherence T_2 enhanced due to the ^{13}C -free nuclear environment. This, combined with the relatively small spectral diffusion of the optical transitions observed in this material, make it appear promising for photonics-based QIP and magnetometry.

■ ASSOCIATED CONTENT

📄 Supporting Information

Additional information and figures. This material is available free of charge via the Internet at <http://pubs.acs.org>.

■ AUTHOR INFORMATION

✉ Corresponding Author

*E-mail: kito@appi.keio.ac.jp.

Notes

The authors declare no competing financial interest.

■ ACKNOWLEDGMENTS

This material is based on work supported in part by Grant-in-Aid for Scientific Research and Project for Developing Innovation Systems by MEXT, in part by Global COE Program “High-Level Global Cooperation for Leading-Edge Platform on

Access Spaces (C12)", in part by the Defense Advanced Research Projects Agency under award no. HR0011-09-1-0006 and the Regents of the University of California.

REFERENCES

- (1) Childress, L.; Taylor, J. M.; Sorensen, A. S.; Lukin, M. D. *Phys. Rev. A* **2006**, *72*, 052330.
- (2) Benjamin, S. C.; Browne, D. E.; Fitzsimons, J.; Morton, J. L. *New J. Phys.* **2006**, *8*, 141.
- (3) Gruber, A.; Dräbenstedt, A.; Tietz, C.; Fleury, L.; Wrachtrup, J.; von Borczyskowski, C. *Science* **1997**, *272*, 2012.
- (4) Jelezko, F.; Gaebel, T.; Popa, I.; Gruber, A.; Wrachtrup, J. *Phys. Rev. Lett.* **2004**, *92*, 076401.
- (5) Santori, C.; Tamarat, P.; Neumann, P.; Wrachtrup, J.; Fattal, D.; Beausoleil, R. G.; Rabeau, J.; Olivero, P.; Greentree, A. D.; Prawer, S.; Jelezko, F.; Hemmer, P. *Phys. Rev. Lett.* **2006**, *97*, 247401.
- (6) Togan, E.; Chu, Y.; Trifonov, A. S.; Jiang, L.; Maze, J.; Childress, L.; Dutt, M. V. G.; Sorensen, A. S.; Hemmer, P. R.; Zibrov, A. S.; Lukin, M. D. *Nature (London)* **2010**, *466*, 730.
- (7) Balasubramanian, G.; Neumann, P.; Twitchen, D.; Markham, M.; Kolesov, R.; Mizuochi, N.; Isoya, J.; Achard, J.; Beck, J.; Tissler, J.; Jacques, V.; Hemmer, P. R.; Jelezko, F.; Wrachtrup, J. *Nat. Mater.* **2009**, *8*, 383.
- (8) Kubo, Y.; Ong, F. R.; Bertet, P.; Vion, D.; Jacques, V.; Zheng, D.; Dreau, A.; Roch, J.-F.; Auffeves, A.; Jelezko, F.; Wrachtrup, J.; Barthe, M. F.; Bergonzo, P.; Esteve, D. *Phys. Rev. Lett.* **2010**, *105*, 140502.
- (9) Fuchs, G. D.; Burkard, G.; Klimov, P. V.; Awschalom, D. D. *Nat. Phys.* **2011**, *7*, 790.
- (10) Zhu, X.; Saito, S.; Kemp, A.; Kakuyanagi, K.; Karimoto, S.; Nakano, H.; Munro, W. J.; Tokura, Y.; Everitt, M. S.; Nemoto, K.; Kasu, M.; Mizuochi, N.; Semba, K. *Nature (London)* **2011**, *478*, 221.
- (11) Balasubramanian, G.; Chan, I. Y.; Kolesov, R.; Al-Hmoud, M.; Tisler, J.; Shin, C.; Kim, C.; Wojcik, A.; Hemmer, P. R.; Krueger, A.; Hanke, T.; Leitenstorfer, A.; Bratschitsch, R.; Jelezko, F.; Wrachtrup, J. *Nature (London)* **2008**, *455*, 648.
- (12) Taylor, J. M.; Cappellaro, P.; Childress, L.; Jiang, L.; Budker, D.; Hemmer, P. R.; Yacoby, A.; Walsworth, R.; Lukin, M. D. *Nat. Phys.* **2008**, *4*, 810.
- (13) Maze, J. R.; Stanwix, P. L.; Hodges, J. S.; Hong, S.; Taylor, J. M.; Cappellaro, P.; Jiang, L.; Dutt, M. V. G.; Togan, E.; Zibrov, A. S.; Yacoby, A.; Walsworth, R. L.; Lukin, M. D. *Nature (London)* **2008**, *455*, 644.
- (14) Acosta, V. M.; Bauch, E.; Ledbetter, M. P.; Santori, C.; Fu, K. M. C.; Barclay, P. E.; Beausoleil, R. G.; Linget, H.; Roch, J. F.; Treussart, F.; Chemerisov, S.; Gawlik, W.; Budker, D. *Phys. Rev. B* **2009**, *80*, 115202.
- (15) Steinert, S.; Dolde, F.; Neumann, P.; Aird, A.; Naydenov, B.; Balasubramanian, G.; Jelezko, F.; Wrachtrup, J. *Rev. Sci. Instrum.* **2010**, *81*, 043705.
- (16) Fu, K.-M. C.; Santori, C.; Barclay, P. E.; Aharonovich, I.; Prawer, S.; Meyer, N.; Holm, A. M.; Beausoleil, R. G. *Appl. Phys. Lett.* **2008**, *93*, 234107.
- (17) Barclay, P. E.; Fu, K.-M. C.; Santori, C.; Beausoleil, R. G. *Opt. Express* **2009**, *17*, 9588.
- (18) Barclay, P. E.; Fu, K.-M. C.; Santori, C.; Beausoleil, R. G. *Appl. Phys. Lett.* **2009**, *95*, 191115.
- (19) Fu, K.-M. C.; Barclay, P. E.; Santori, C.; Faraon, A.; Beausoleil, R. G. *New J. Phys.* **2011**, *13*, 055023.
- (20) Faraon, A.; Barclay, P. E.; Santori, C.; Fu, K.-M. C.; Beausoleil, R. G. *Nat. Photonics* **2011**, *5*, 301.
- (21) Santori, C.; Barclay, P. E.; Fu, K.-M. C.; Beausoleil, R. G. *Phys. Rev. B* **2009**, *79*, 125313.
- (22) Fu, K.-M. C.; Santori, C.; Barclay, P. E.; Beausoleil, R. G. *Appl. Phys. Lett.* **2010**, *96*, 121907.
- (23) Fu, K.-M. C.; Santori, C.; Faraon, A.; Beausoleil, R. G.; Barclay, P. E.; Twitchen, D. J.; Markham, M. L. *Proc. SPIE* **2011**, *7948*, 79480S.
- (24) Robledo, L.; Childress, L.; Bernien, H.; Hensen, B.; Alkemade, P. F. A.; Hanson, R. *Nature (London)* **2011**, *477*, 574.
- (25) Buckley, B. B.; Fuchs, G. D.; Bassett, L. C.; Awschalom, D. D. *Science* **2010**, *330*, 1212.
- (26) Naydenov, B.; Reinhard, F.; Lammler, A.; Richter, V.; Kalish, R.; D'Haenens-Johansson, U. F. S.; Newton, M.; Jelezko, F.; Wrachtrup, J. *Appl. Phys. Lett.* **2010**, *97*, 242511.
- (27) Manson, N. B.; Harrison, J. P. *Diamond Relat. Mater.* **2005**, *14*, 1705.
- (28) A. Dréau, Lesik, M.; Rondin, L.; Spinicelli, P.; Arcizet, O.; Roch, J.-F.; Jacques, V. arXiv:cond-mat.mes-hall/1108.0178v1 [cond-mat.mes-hall], 2011, (accessed March 14, 2012).
- (29) Smeltzer, B.; Childress, L.; Gali, A. *New J. Phys.* **2011**, *13*, 025021.
- (30) Smeltzer, B.; McIntyre, J.; Childress, L. *Phys. Rev. A* **2009**, *80*, 050302.
- (31) He, X.-F.; Manson, N. B.; Fisk, P. T. H. *Phys. Rev. B* **1993**, *47*, 8816.
- (32) Felton, S.; Edmonds, A. M.; Newton, M. E.; Martineau, P. M.; Fisher, D.; Twitchen, D. J.; Baker, J. M. *Phys. Rev. B* **2009**, *79*, 075203.
- (33) Zhao, N.; Ho, S.-W.; Liu, R.-B. arXiv:cond-mat.mes-hall/1108.2343v1 [cond-mat.mes-hall], 2011, (accessed March 14, 2012).
- (34) Acosta, V. M.; Bauch, E.; Ledbetter, M. P.; Waxman, A.; Bouchard, L.-S.; Budker, D. *Phys. Rev. Lett.* **2010**, *104*, 070801.
- (35) Mizuochi, N.; Neumann, P.; Rempp, F.; Beck, J.; Jacques, V.; Siyushev, P.; Nakamura, K.; Twitchen, D. J.; Watanabe, H.; Yamasaki, S.; Jelezko, F.; Wrachtrup, J. *Phys. Rev. B* **2009**, *80*, 041201.
- (36) Gaebel, T.; Domhan, M.; Popa, I.; Wittmann, C.; Neumann, P.; Jelezko, F.; Rabeau, J. R.; Stavrias, N.; Greentree, A. D.; Prawer, S.; Meijer, J.; Twamley, J.; Hemmer, P. R.; Wrachtrup, J. *Nat. Phys.* **2006**, *2*, 408.